Faceting, Grain Growth, and Crack Healing in Alumina:

Supporting Information

Pankaj Rajak[12], Rajiv K. Kalia[1234*], Aiichiro Nakano[1243], and Priya Vashishta[1234]*

[1]Collaboratory for Advanced Computing and Simulations, [2]Department of Chemical Engineering & Materials Science, [3]Department of Computer Science, [4]Department of Physics & Astronomy, University of Southern California, Los Angeles, CA, 90089-0242, USA

[*]Corresponding authors: rajak@usc.edu, rkalia@usc.edu

Reactive Molecular Dynamics Simulations: Initial and Boundary Conditions

The initial setup of the RMD simulation is shown schematically in Figure S1(a) and, for reference, crystalline planes of α-Al_2O_3 normal to the basal (0001) and prism ($2\bar{1}10$) planes are shown in Figs. S1 (b) and (c), respectively. The alumina matrix has a pre-crack of length 15nm and rows of SiC/SiO_2 nanoparticles (NPs) ahead of the pre-crack front. Four sets of simulations were done corresponding to 1, 2, 3, and 4 rows of NPs. The initial separation of the first, second, third, and fourth row of NPs from the pre-crack were 4.5 nm, 50 nm, 85 nm, and 115 nm respectively. Strain was applied incrementally in the *y* direction. At each increment, the system was expanded in the *y* direction by 0.1 nm over a duration of 10 ps and then relaxed for 60 ps. During relaxation, Al and O atoms within 2 nm from the boundaries in the *y* direction were kept fixed. Under strain, the crack propagates from right to left along the *x* axis. In order to avoid spurious effects arising from the interaction between the crack front and stress waves reflected from the boundaries normal to the *x* axis, atoms within 2 nm from the boundaries were held fixed

and atoms between 2 – 4 nm from the boundaries normal to the *x* axis were damped with Langevin dynamics.

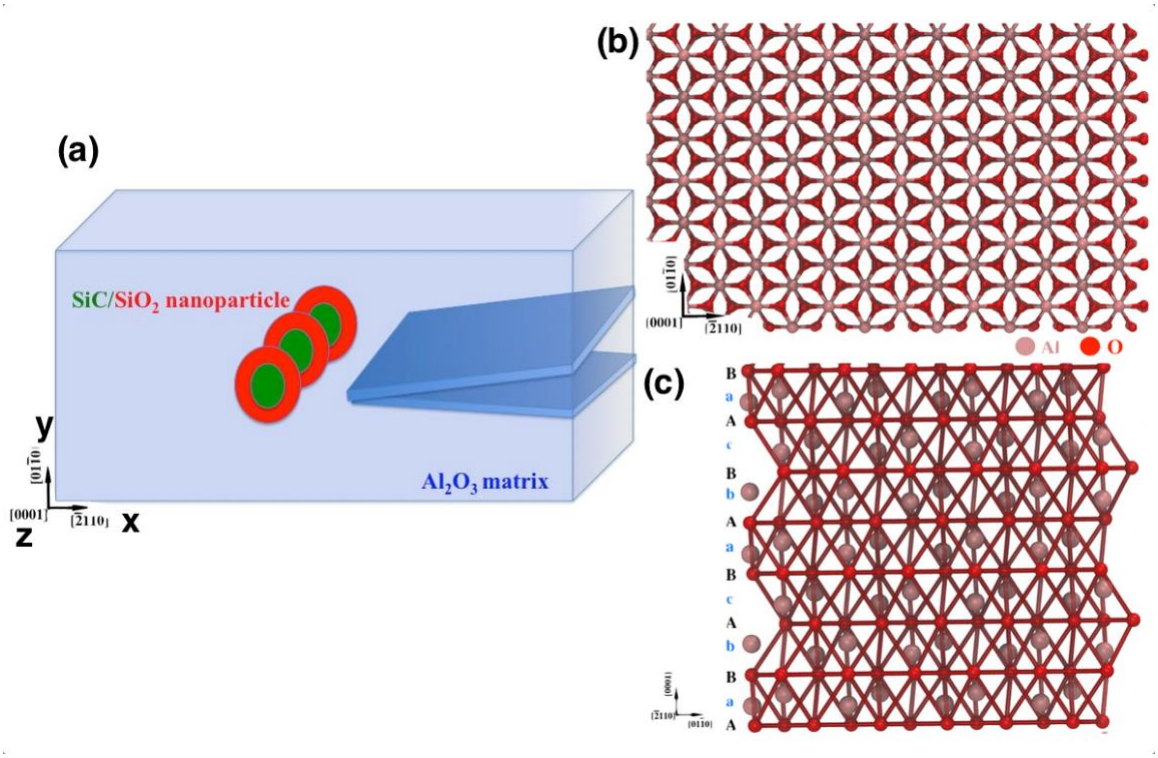

Figure S1: (a) *Schamatic of mode 1 fracture of Al_2O_3 matrix (light blue) containing a pre-crack (dark blue) and a row of n-SiC (green) with SiO_2 shells (red). Atomic arrangements in (b) basal and (c) prism planes of Al_2O_3*

Stress-Strain Curve and Nanoindentation Response of Al_2O_3 Containing SiC/SiO_2 Core-Shell Nanoparticles

We performed MD simulations on two systems of dimensions 180nm × 40nm × 18nm and 70nm × 40nm ×18nm. Here we report results for the larger system. We find the same crack self-healing mechanism and grain growth in the smaller system as well. In the case of pure α-Al_2O_3, both the smaller and larger systems fracture at a strain of 3.5%. In the presence of a row of SiC/a-SiO_2 nanoparticles, both systems exhibit grain nucleation at a strain of 3.5%.

Figure S2 (a) shows the stress-strain curve for pure α-Al_2O_3 and Al_2O_3 containing four rows of silica coated SiC nanoparticles. The results indicate that the crack-healed nanocomposite with four rows of SiC/SiO_2 core/shell nanoparticles does not fracture until the strain exceeds 5%. With additional nanoparticles, the nanocomposite can withstand higher strains.

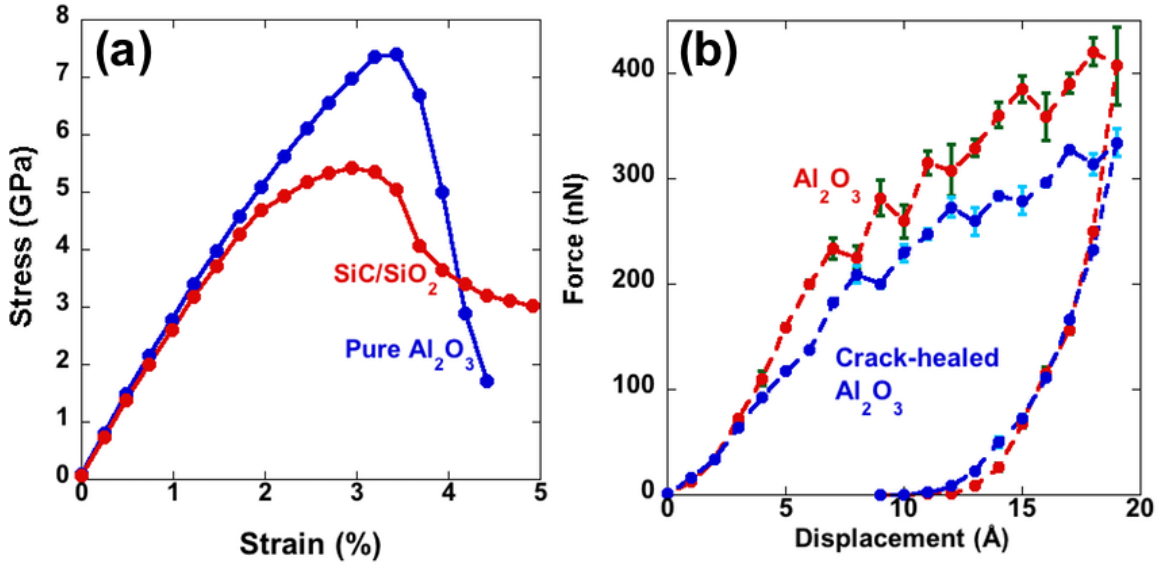

Figure S2: (a) *Stress-Strain curve for an Al_2O_3 composite with four rows of SiC/SiO_2 nanoparticles and for pure Al_2O_3 system during mode 1 fracture. (b) Load-displacement curves for pure α-Al_2O_3 (blue) and Al_2O_3 composite (red) after crack healing.*

To gain further insight into the mechanical behavior of the Al_2O_3 composite after crack healing, we have performed nanoindentation at room temperature using MD simulation. We use a spherical indenter of radius 2 nm to indent a region of the alumina matrix between two adjacent rows of a-SiO_2 coated SiC nanoparticles. The size of the indented region is $15nm \times 15nm \times 15nm$. First, the composite is quenched to 25°C from 1,426°C in the NPT ensemble and then relaxed in the NVE ensemble. The indentation test is carried out in two stages: (1) the indenter is moved towards the composite by 0.1

nm in 10 ns, and (2) the entire system is relaxed for 40 ns without moving the indenter. The force on the indenter is computed by taking averages over 10 ns. The unloading phase has the same schedule as the loading phase. We have also performed nanoindentation on pure α-Al_2O_3 using the same indenter and following the same schedule. In both systems, the indenter is moved along the $[01\bar{1}0]$ direction. Figure S2 (b) shows that load-displacement curves for α-Al_2O_3 and self-healed Al_2O_3 composite nearly overlap. The calculated hardness of the Al_2O_3 composite after self-healing is close to that of pure α-Al_2O_3 (40 GPa), which is in good agreement with the experimental value.[1]

Our results are consistent with experiments of Ando *et al*.[2] They introduced indentation cracks on crack-healed samples and performed three-point bending experiment as a function of temperature. They found fracture outside the crack-healed zones in alumina nanocomposites. In contrast, fracture initiated just below indentation cracks in samples without crack healing treatment. Ando *et al*. also found that bending strengths of crack-healed Al_2O_3 composites were higher than the bending strength of pure Al_2O_3 at room temperature. They conjectured that the crack-healing mechanism involved the formation of silica shells around n-SiC by oxidation of Si with atmospheric oxygen followed by diffusion of liquid silica into cracks. The exothermic heat and volume expansion associated with the oxidation of n-SiC are believed to play important roles in accelerating crack healing by diffusion of silica into the damaged zone. Our simulation results provide direct evidence for the crack-healing mechanism in Al_2O_3 containing silica coated silicon carbide nanoparticles.

Interaction Potentials

The interatomic potentials for Al_2O_3, SiO_2, and SiC have the same functional form. They consist of two-body and three-body terms:

$$E_{tot} = \sum_{i<j} V_{ij}^{(2)}(r_{ij}) + \sum_{i<j<k} V_{ijk}^{(3)}(\overrightarrow{r_{ij}}\overrightarrow{r_{ik}}) \quad (1)$$

where r_{ij} is the separation between atoms i and j positioned at $\bar{r}_i$ and $\bar{r}_j$, respectively, and $\bar{r}_{ij} = \bar{r}_i - \bar{r}_j$. The two-body potential has steric repulsion, screened Coulomb, charge-dipole, and van der Waals $1/r^6$ terms:

$$V_{ij}^2(r) = \frac{H_{ij}}{r^{\eta_{ij}}} + \frac{Z_i Z_j}{r} e^{-\frac{r}{r_{is}}} - \frac{D_{ij}}{2r^4} e^{-\frac{r}{r_{4s}}} - \frac{w_{ij}}{r^6} \quad (2)$$

The expression for the three-body potential is

$$V_{ijk}^{(3)}(\overrightarrow{r_{ij}}\overrightarrow{r_{ik}}) = B_{ijk} \exp\left(\frac{\xi}{r_{ij}-r_0} + \frac{\xi}{r_{ik}-r_0}\right) \frac{(cos\theta_{ijk}-cos\theta_0)^2}{1+C_{jik}(cos\theta_{ijk}-cos\theta_0)^2} \quad (r_{ij}, r_{ik} \leq 0) \quad (3)$$

In Eq. (2) H_{ij} is the strength and η_{ij} is the exponent of steric repulsion, Z_i is the effective charge, D_{ij} represents the charge-dipole strength, and w_{ij} is the strength of van-der Waals attraction. r_{1s} and r_{4s} are the screening lengths for Coulomb and charge-dipole interactions, respectively. In Eq. (3), B_{ijk} is the strength of the three-body interaction, ξ and C_{ijk} are constants and, θ_{ijk} is the angle between atom $\bar{r}_{ji}$ and $\bar{r}_{jk}$.

Next, we describe how SiC, SiO_2 and Al_2O_3 force fields were validated by comparing MD results with experimental data and quantum mechanical (QM) calculations based on density functional theory (DFT).

SiC Force Field Validation: The force field was validated by comparing MD simulation results with DFT calculations and experimental measurements of elastic constants, melting temperature, vibrational density of states, and specific heat.[3,4] Table 1 lists our results for elastic moduli, bulk modulus and Poisson's ratio and the corresponding results from DFT calculations and experimental measurements.

Table 1: *Comparison between MD results based on the Vashishta force field (VFF), DFT calculations, and experimental measurements of elastic moduli, bulk modulus and Poisson's ratio of 3C-SiC.*

3C-SiC	Vashishta Potential	Expt.	DFT
B (GPa)	225.1	225	224.9
C_{11} (GPa)	390.0	390.0	401.9
C_{12} (GPa)	142.7	142	136.4
C_{44} (GPa)	191.0	256	255.7
Young's Modulus (GPa)	313.6	314.2, 392-694	456.6
Shear Modulus (GPa)	123.7	124, 192	196.5
Poison ratio (ν)	0.268	0.267, 0.168	0.1616

The SiC force field was subjected to more stringent tests as well. One of the validation tests involved pressure-induced phase transformation from the zinc blend-to-rock salt structure. It is noteworthy that our MD simulation predicted a new mechanism for the structural transformation, which was later confirmed by DFT calculation.[3, 5] We observed the transition around 100 GPa, which is in good agreement DFT calculation and experimental data. Additional validation tests for SiC included (i) the structure of amorphous SiC; (ii) unstable stacking fault energy for the (111) glide plane in the $[10\bar{1}]$ direction; and (iii) anisotropic fracture toughness of 3C-SiC.

We also used the force field in an MD simulation of indentation of nanocrystalline SiC.[6] We found unusual deformation mechanisms resulting from the coexistence of brittle grains and soft amorphous grain boundary phases in nanocrystalline SiC. We discovered

a crossover phenomenon from continuous intergranular to discrete intragrain response due to the coexistence of hard crystalline grains and soft amorphous grain boundary phases. The calculated hardness, 27.5 GPa, is in good agreement with experimental "superhardness" value which ranges between 30 and 50 GPa for grain sizes 5-20 nm.[7,8]

Silica Force Field Validation: The SiO_2 force field correctly describes the structural and mechanical properties of amorphous silica and melting behavior of silica.[9] Our MD results agree very well with neutron scattering data for static structure factor of amorphous SiO_2. The calculated values of elastic moduli of a-SiO_2 (Young's modulus = 66.9 GPa, Bulk modulus = 39.2 GPa, Poisson's ratio = 0.22) are in good agreement with experiments and the calculated fracture toughness is well within the range of experimental values (0.8-1.2 $MPa \cdot m^{1/2}$).[10] We also performed nanoindentation simulations and found that the MD result for hardness of amorphous silica (10.6 GPa) is close to the experimental value (10 GPa).[11]

Alumina Force Field Validation: The force field for Al_2O_3 can successfully describe structural and mechanical properties of crystalline and amorphous phases and melting behavior of α-Al_2O_3.[12-15] Our results for neutron and x ray static structure factors are in good agreement with experiments. Table 2 shows that MD results for bulk modulus, Poisson's ratio and elastic moduli compare very well with experimental measurements.[4, 12] We also performed nanoindentation simulations and found the hardness value is in agreement with experimental value.[16]

We have calculated the ground state energies of corundum and bixbyite structures using the Vashishta potential. The ground state energy of the corundum (-6.35 eV/atom) agrees very well with the experimental value, and it is slightly lower than that of bixbyite (-6.27

eV/atom).

Table 2: *Comparison between MD results based on the Vashishta force field, DFT calculations, and experimental measurements of elastic moduli, bulk modulus and Poisson's ratio of α-Al_2O_3.*

Al_2O_3	Vashishta Potential	Expt.	DFT
B (GPa)	253	255	246.9
C_{11} (GPa)	523	498	476.8
C_{12} (GPa)	147	164	157.6
C_{13} (GPa)	129	117	119.4
C_{14} (GPa)	7.5	-23	19.4
C_{33} (GPa)	427	502	476.6
C_{44} (GPa)	135	147	145.5
C_{66} (GPa)	174	167	159.6
Poison ratio (ν)	0.22	0.231	0.2356

To test the transferability of the force field, we examined deformation mechanisms in α-Al_2O_3 under hypervelocity impact using MD simulations. We observed a wide range of deformations such as basal and pyramidal slips and basal and rhombohedral twins, all of which show good agreement with experimental and theoretical results. From the hypervelocity impact simulations, we estimated the fracture toughness of α-Al_2O_3 which is within the range of experimental values (2.2 - 2.5 MPa•$m^{1/2}$). Our MD simulation of impact damage shows a phase transformation in alumina,[13, 15] akin to the experimentally observed contact-induced phase transformation.[13, 17,18]

We use an interpolation scheme to describe the force field at the alumina-silica interface. We have used such a scheme in MD simulation studies of fracture in a Si_3N_4 matrix containing silica coated silicon carbide fibers.[19] Similar interpolation schemes have been successfully used to describe interfacial phenomena in InAs/GaAs[20,21] and silica/water.[22]

Comparison of Vashishta Force Field (VFF) for SiC-SiO_2 with ReaxFF

The VFF has a simpler functional form and fewer training parameter than the reactive force fields ReaxFF we used in a recent MD simulation study of oxidation dynamics of SiC nanoparticles.[23] We have tested the accuracy of VFF against ReaxFF on a system consisting of a SiC nanoparticle (diameter 7 nm) embedded in an amorphous SiO_2 shell of dimensions $12nm \times 12nm \times 12nm$. First, we perform a VFF-MD simulation to heat and thermalize the system at 1,426° C. Next, we quench the system to room temperature and observe the formation of an amorphous silica (a-SiO_2) shell around the SiC nanoparticle. Taking a configuration of the system at room temperature, we switch the force field from VFF to ReaxFF and perform MD simulation to check the stability, structure and dynamics of the system. The force-field switching does not alter the stability or the basic structure of the n-SiC/a-SiO_2 system. We find that atomic trajectories of VFF-MD simulation are close to those of ReaxFF-MD simulation. The mean-square displacements of Si and C atoms in the SiC core and of Si and O atoms in the a-SiO_2 shell are less than 0.50 $Å^2$ and 0.35 $Å^2$, respectively.

Crack Healing in Al_2O_3 by Silica Diffusion

The effect of applied strain on the separation between the crack front and NPs indicates how NPs arrest crack growth. Figure S3 (a) shows that the separation $d_{C\text{-}P}$ between the crack front and two NPs in the path of the advancing crack decreases with the applied

strain. Initially, the size of the two NPs is 7 nm and the separation between the crack tip and NPs $d_{C\text{-}P}$ is 4.5 nm. $d_{C\text{-}P}$ decreases to 3.5 nm as the applied strain ε_{yy} is increased to 2%. With further increase in strain, $d_{C\text{-}P}$ decreases dramatically and vanishes at ε_{yy} = 4%. Figure S3 (b) shows that the stress component $\Delta\sigma_{xx}$ drops rapidly when the NPs arrest the crack growth.

The applied strain also affects the inter NP distance, $d_{P\text{-}P}$, in much the same way as it does $d_{C\text{-}P}$, the distance between the crack front and NPs. The initial separation between the two NPs of diameter 7 nm is 1.5 nm. $d_{P\text{-}P}$ decreases as the strain is raised to 1.5% and vanishes when the two NPs coalesce at a strain of 2.7%. The two NPs form a neck through which Si and O atoms begin to diffuse. The width of the neck and Si and O diffusion between the NPs increase with the applied strain.

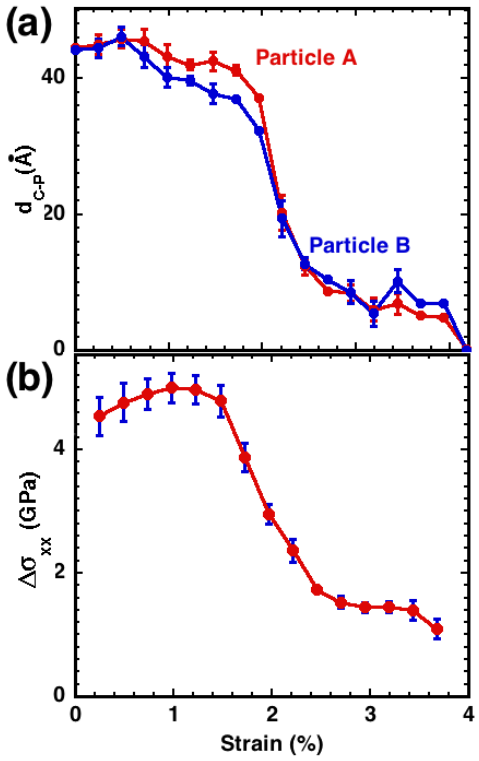

Figure S3: *(a) Distance between crack-front and NPs in an Al_2O_3 matrix containing a row of two n-SiC/SiO_2 nanoparticles. The initial separation between the crack and nanoparticles is 4.5 nm and the*

diameter of each nanoparticle is 7 nm. (b) Strain dependence of $\boldsymbol{\Delta\sigma_{xx}}$ *, which is the difference in the stress at the crack tip and NPs.*

Structural Analysis Inside Secondary Amorphous Grains in Alumina

Structural correlations reveal that the alumina matrix ahead of the NPs is mostly unaffected by the applied strain. Figure S4 (a) shows two regions of the alumina matrix in which we have calculated Al-O radial distribution functions, $g(r)$, and O-Al-O and Al-O-Al bond angle distributions at different values of the applied strain, ε_{yy}. Figures S4 (b) and (c) show that $g(r)$ are nearly the same at $\varepsilon_{yy} = 0$ and $\varepsilon_{yy} = 4.5\%$. Similarly, we do not observe any noticeable differences between O-Al-O bond angle distributions at $\varepsilon_{yy} = 0$ and $\varepsilon_{yy} = 4.5\%$. However, in the Al-O-Al bond angle distribution the two distinct peaks at 90˚ and 130˚ at $\varepsilon_{yy} = 0$ have merged into one broad peak at $\varepsilon_{yy} = 4.5\%$.

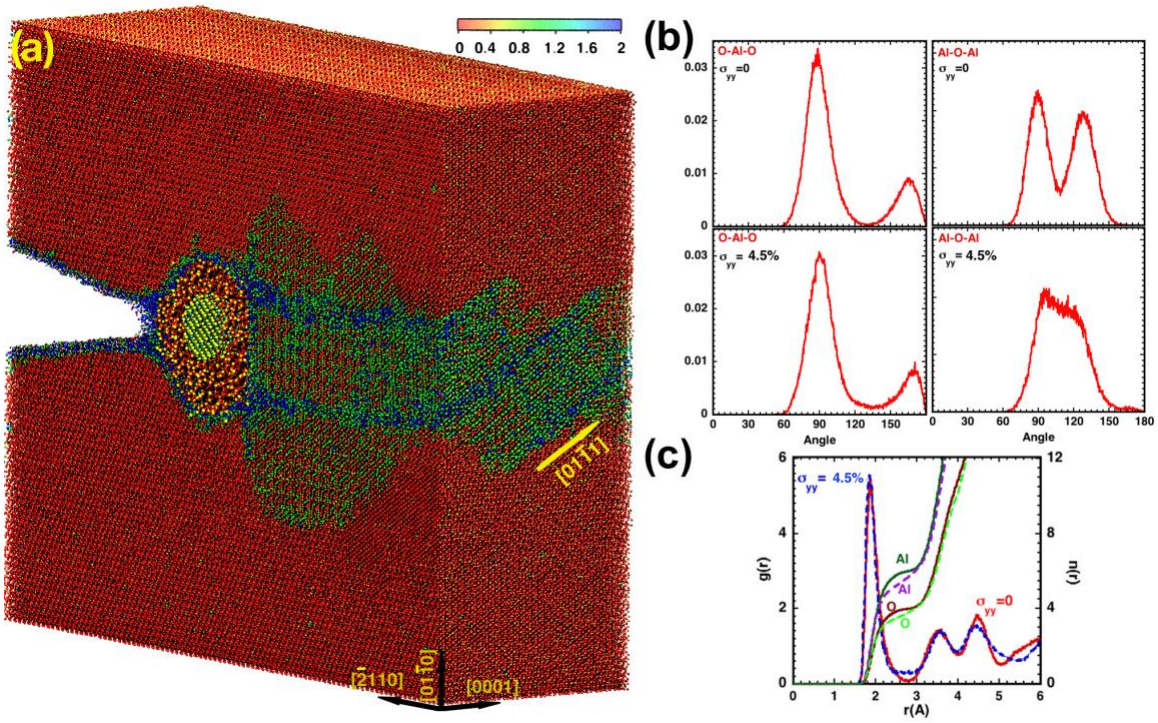

Figure S4: *(a) Local deformation analysis of the deformed region in Al_2O_3 matrix at 4.5% strain. (b) Al-O-Al and O-Al-O bond angle distributions in the deformed region of alumina. (c) Radial distribution function*

g(r) for Al-O and coordination number n(r) in the deformed region. Here dotted lines are g(r) and n(r) plots in Al_2O_3 matrix at 0% strain and solid lines in the deformed region of Al_2O_3 matrix at 4.5% strain.

Supporting Movies:

Movie S1: Shows nucleation and grain growth at the interface of an Al_2O_3 –SiC/SiO_2 nanoparticle in the Al_2O_3 matrix containing two rows of n-SiC/SiO_2 nanoparticles. Black spheres are Al and O atoms of Al_2O_3 and grey, yellow and red atoms are C, Si and O atoms of a n-SiC/SiO_2 nanoparticle. Atoms in secondary grains are blue and green. The grain boundary between primary and secondary Al_2O_3 grains are shown in light green and cyan.

Movie S2: Shows stress distribution and local damage inside the Al_2O_3 matrix containing 2 rows of NPs as a function of applied strain. Stress distribution and local damage is shown on a cross-section of Al_2O_3 at y = 20 nm. Here yellow and red are silicon and oxygen atoms, respectively. Al_2O_3 atoms with D^2_{min} value less than 0.25 are shown in black and the remaining Al_2O_3 atoms are colored by their D^2_{min} values.

Movie S3: Nucleation and crack growth along $[01\bar{1}1]$ direction of the prism plane of Al_2O_3 containing 2 rows of NPs as a function of applied strain. Here Al_2O_3 atoms are black and Si and O atoms of NPs are yellow and red, respectively. Atoms near the crack surface or in the damage zone are colored by their D^2_{min} values.

Movie S4: Damage zone formation in Al_2O_3 containing 4 rows of NPs as a function of applied strain. Here nanovoids inside Al_2O_3 are healed by silica and there is no crack formation inside the Al_2O_3 matrix. Atoms in Al_2O_3 are black and Si and O atoms in NPs

are yellow and red, respectively. Atoms near the crack surface or in the damage zone are colored by their D^2_{min} values.

References:

1. Scholz, T.; Schneider, G. A.; Muñoz-Saldaña, J.; Swain, M. V., Fracture Toughness from Submicron Derived Indentation Cracks. *Appl. Phys. Lett.* **2004,** *84*, 3055-3057.
2. Ando, K.; Kim, B. S.; Chu, M. C.; Saito, S.; Takahashi, K., Crack-Healing and Mechanical Behaviour of Al_2O_3/SiC Composites at Elevated Temperature. *Fatigue Fract. Eng. Mater. Struct.* **2004,** *27*, 533-541.
3. Vashishta, P.; Kalia, R. K.; Nakano, A.; Rino, J. P., Interaction Potential for Silicon Carbide: A Molecular Dynamics Study of Elastic Constants and Vibrational Density of States for Crystalline and Amorphous Silicon Carbide. *J. Appl. Phys.* **2007,** *101*, 103515.
4. Yao, H.; Ouyang, L.; Ching, W.-Y., Ab Initio Calculation of Elastic Constants of Ceramic Crystals. *J. Am. Ceram. Soc.* **2007,** *90*, 3194-3204.
5. Shimojo, F.; Ebbsjö, I.; Kalia, R. K.; Nakano, A.; Rino, J. P.; Vashishta, P., Molecular Dynamics Simulation of Structural Transformation in Silicon Carbide under Pressure. *Phys. Rev. Lett.* **2000,** *84*, 3338-3341.
6. Chen, H.-P.; Kalia, R. K.; Nakano, A.; Vashishta, P.; Szlufarska, I., Multimillion-Atom Nanoindentation Simulation of Crystalline Silicon Carbide: Orientation Dependence and Anisotropic Pileup. *J. Appl. Phys.* **2007,** *102*, 063514.
7. Cha, Y. C.; Kim, G.; Doerr, H. J.; Bunshah, R. F., Effects of Activated Reactive Evaporation Process Parameters on the Microhardness of Polycrystalline Silicon Carbide Thin Films. *Thin Solid Films* **1994,** *253*, 212-217.
8. Liao, F.; Girshick, S. L.; Mook, W. M.; Gerberich, W. W.; Zachariah, M. R., Superhard Nanocrystalline Silicon Carbide Films. *Appl. Phys. Lett.* **2005,** *86*, 171913.

9. Vashishta, P.; Kalia, R. K.; Rino, J. P.; Ebbsjo, I., Interaction Potential for SiO_2: A Molecular-Dynamics Study of Structural Correlations. *Phys. Rev. B* **1990,** *41*, 12197-12209.
10. Ken-ichi, N.; Yi-Chun, C.; Wang, W.; Rajiv, K. K.; Aiichiro, N.; Priya, V.; Lin, H. Y., Interaction and Coalescence of Nanovoids and Dynamic Fracture in Silica Glass: Multimillion-to-Billion Atom Molecular Dynamics Simulations. *J. Phys. D.* **2009,** *42*, 214011.
11. Nomura, K.; Chen, Y.; Kalia, R. K.; Nakano, A.; Vashishta, P., Defect Migration and Recombination in Nanoindentation of Silica Glass. *Appl. Phys. Lett.* **2011,** *99*, 111906.
12. Vashishta, P.; Kalia, R. K.; Nakano, A.; Rino, J. P., Interaction Potentials for Alumina and Molecular Dynamics Simulations of Amorphous and Liquid Alumina. *J. Appl. Phys.* **2008,** *103*, 083504.
13. Zhang, C.; Kalia, R. K.; Nakano, A.; Vashishta, P.; Branicio, P. S., Deformation Mechanisms and Damage in α-Alumina under Hypervelocity Impact Loading. *J. Appl. Phys.* **2008,** *103*, 083508.
14. Zhang, C.; Kalia, R. K.; Nakano, A.; Vashishta, P., Hypervelocity Impact Induced Deformation Modes in α-Alumina. *Appl. Phys. Lett.* **2007,** *91*, 071906.
15. Zhang, C.; Kalia, R. K.; Nakano, A.; Vashishta, P., Fracture Initiation Mechanisms in α-Alumina under Hypervelocity Impact. *Appl. Phys. Lett.* **2007,** *91*, 121911.
16. Nishimura, K.; Kalia, R. K.; Nakano, A.; Vashishta, P., Nanoindentation Hardness Anisotropy of Alumina Crystal: A Molecular Dynamics Study. *Appl. Phys. Lett.* **2008,** *92*, 161904.
17. Mashimo, T.; Tsumoto, K.; Nakamura, K.; Noguchi, Y.; Fukuoka, K.; Syono, Y., High-Pressure Phase Transformation of Corundum (α-Al_2O_3) Observed under Shock Compression. *Geophys. Res. Lett.* **2000,** *27*, 2021-2024.
18. Duan, W.; Wentzcovitch, R. M.; Thomson, K. T., First-Principles Study of High-Pressure Alumina Polymorphs. *Phys. Rev. B* **1998,** *57*, 10363-10369.
19. Nakano, A.; Kalia, R. K.; Vashishta, P., Scalable Molecular-Dynamics, Visualization, and Data-Management Algorithms for Materials Simulations. *Comput. Sci. Eng.* **1999,** *1*, 39-47.

20. Su, X.; Kalia, R. K.; Nakano, A.; Vashishta, P.; Madhukar, A., Critical Lateral Size for Stress Domain Formation in InAs/GaAs Square Nanomesas: A Multimillion-Atom Molecular Dynamics Study. *Appl. Phys. Lett.* **2001,** *79*, 4577-4579.
21. Su, X.; Kalia, R. K.; Nakano, A.; Vashishta, P.; Madhukar, A., Million-Atom Molecular Dynamics Simulation of Flat InAs Overlayers with Self-Limiting Thickness on GaAs Square Nanomesas. *Appl. Phys. Lett.* **2001,** *78*, 3717-3719.
22. Shekhar, A.; Nomura, K.; Kalia, R. K.; Nakano, A.; Vashishta, P., Nanobubble Collapse on a Silica Surface in Water: Billion-Atom Reactive Molecular Dynamics Simulations. *Phys. Rev. Lett.* **2013,** *111*, 184503.
23. Nomura, K.; Kalia, R. K.; Li, Y.; Nakano, A.; Rajak, P.; Sheng, C.; Shimamura, K.; Shimojo, F.; Vashishta, P., Nanocarbon Synthesis by High-Temperature Oxidation of Nanoparticles. *Sci. Rep.* **2016,** *6*, 24109.